Supplemental Material for "Cenozoic delamination of the southwestern Yangtze Craton owing to densification during subduction and collision"

Text S1. Analytical methods

1.1. Whole-rock major and trace elements

The samples for bulk-rock elemental analyses were crushed to coarse chips and fresh pieces were hand-picked. The rock chips were rinsed twice with MiliQ water, dried, and then powdered to ~200 mesh size in an agate mortar and pestle set that was free from metal contamination. Major-element oxides were analyzed on fused glass beads using a Rigaku RIX 2000 X-ray fluorescence spectrometer at the State Key Laboratory of Isotope Geochemistry, Guangzhou Institute of Geochemistry, Chinese Academy of Sciences (SKLaBIG GIG CAS). Interference-corrected spectra were converted to oxide-concentrations using a calibration curve consisting of 36 standard samples. The analytical procedures are described in detail by Li et al. (2005), and the analytical uncertainties are 1%–5%. Trace elements, including rare earth elements (REEs), were analyzed by inductively coupled plasma–mass spectrometry (ICP–MS), using a Perkin-Elmer ELAN 6000 instrument at the SKLaBIG GIG CAS, following the procedures described by Li et al. (2006). About 40 mg of each powdered sample was dissolved in a high-pressure Teflon bomb for 2 days at 190 ℃ using $HF+HNO_3+HClO_4$ (1:1:0.2) mixtures. Analytical precisions for most elements are better than 5%. Major and trace element concentrations are given in Table S1.

1.2. Olivine, spinel, and clinopyroxene major elements

In situ major element analyses of olivines and clinopyroxenes were obtained using a Cameca SXFive FE Electron Probe Microanalyzer (EPMA) at the SKLaBIG GIG CAS, and a JEOL JXA-8230 EPMA at the Key Laboratory of Mineralogy and Metallogeny in Guangzhou Institute of Geochemistry, Chinese Academy of Sciences (KLMM GIG CAS). The operating conditions for olivine analysis are a 15 kV accelerating voltage, a 100 nA beam current, and a beam size of 5 μm. Standards used for olivine analysis were olivine (Si, Mg, Fe), jadeite (Al), rhodonite (Mn), diopside (Ca), pentlandite (Ni), rutile (Ti), Chromite (Cr), Albite (Na), and monazite (P). During the measurement of olivine, the MongOl olivine (Batanova et al., 2015) was used to monitor the accuracy of the measurements as well as machine drift error. Major-element data for olivine samples and monitoring standards are given in Table S2. The operating conditions for clinopyroxene analysis are 15 kV, a 20 nA, and a 1 μm beam. Calibration standards for clinopyroxene analyses were jadeite (Na, Al), diopside (Si, Mg, Ca), orthoclase (K), rutile (Ti), Cr_2O_3 (Cr), hematite (Fe), and rhodonite (Mn). Analyzed major element compositions of clinopyroxene are reported in Tables S3.

In situ major element contents of spinel inclusions in olivine were analyzed using a JEOL JXA-8230 EPMA at the KLMM GIG CAS. The backscattered electron (BSE) images were used for the selection of homogeneous cores (Fig. S2). The operating conditions are 15 kV, 20 nA and a 1 μm beam. Standards for spinel analyses were olivine (Si, Mg), chromite (Cr, Al), magnetite (Fe),

rhodonite (Mn), pentlandite (Ni), and rutile (Ti). At the beginning and end of each electron microprobe session, we measured spinel standards with $Fe^{3+}/\Sigma Fe$ ratios previously characterized by Mössbauer spectroscopy. Major-element data for spinel samples and standards are given in Table S4 and S7, respectively.

1.3. Olivine oxygen isotope

Olivine grains were hand-picked using a binocular microscope. The selected grains were mounted in epoxy and polished. Microphotographs under both transmitted and reflected light were used to select fracture-free, large grains for chemical analysis by electron microprobe. The backscattered electron (BSE) images (Fig. S2) were used for target selection during *in situ* oxygen isotope analysis by a Cameca IMS-1280-HR SIMS (secondary ion mass spectrometry) at the SKLaBIG GIG CAS. The beam size was about 10-15 μm. The analytical procedures, instrument conditions, calibration and data reduction are the same as given in Yang et al. (2018). Five unknown and two standard $\delta^{18}O$ measurements were run in bracketed mode. Measured $^{18}O/^{16}O$ was normalized using the Vienna Standard Mean Ocean Water composition (VSMOW, $^{18}O/^{16}O$ = 0.0020052). The measured oxygen isotopic data were corrected for instrumental mass fractionation (IMF) using the Jingyu olivine standard (06JY34; Fo = 91.5) with a recommended value of 5.25 ±0.07‰ (Tang et al., 2019). The experience from the Cameca IMS 1270, 1280 and 1290 labs worldwide indicates that matrix effects resulting from variable Mg# in olivine on the measured oxygen isotope ratios is not significant, provided that the olivine is characterized by Fo values ranging from 60 to 100 (e.g., Bindeman et al., 2008; Isa et al., 2017; Tang et al., 2019). For example, Bindeman et al. (2008) observed a systematic difference of IMF for San Carlos (Fo = 90) and CI114 (Fo = 74) olivines of 0.12‰, which translates to 0.0075‰ of IMF per each Fo number. Accordingly, difference of IMF for olivine phenocrysts (Fo = 81-94) used in this study is less than 0.1‰, which is negligible and within error of our measurements. To monitor the external uncertainties, a second olivine standard (06JY29; Fo = 91.2) was alternately analyzed as an unknown together with other unknown olivines. Measurements on 06JY29 olivine yielded a $\delta^{18}O$ value of 5.26 ±0.17 ‰ (1σ, n = 16; Table S5), which is within error of the recommended value of 5.30 ±0.13 ‰ (Tang et al., 2019). Olivine oxygen isotopic data are presented in Table S5.

Text S2. Calculation methods

2.1. Mantle-melt barometers

The pressures of mantle melting can be estimated using primary melt compositions (Lee et al., 2009; Sun and Dasgupta, 2020). Primary magma compositions should be calculated by correcting for low pressure fractionation. It is best to choose primitive (e.g., least fractionated; MgO > 9 wt.%) magmas that have fractionated along olivine-control lines (Lee et al., 2009). We could estimate the primary melt compositions by adding equilibrium olivine increments back into the differentiated magma or by subtracting accumulated olivine from the primitive magma, until the magma achieves Fe/Mg exchange equilibrium with mantle olivine. There are three parameters that can influence the corrected compositions of primary melts and hence the results of pressure calculations (Lee et al., 2009): (1) the Fe-Mg exchange coefficient ($K_D[Fe/Mg]^{ol/liq}$) between olivine and liquid; (2) the Fo value of mantle olivine; (3) the melt $Fe^{3+}/\Sigma Fe$ ratio which increases with oxygen fugacity (fO_2). The mantle olivines in equilibrium with the Dali and Yanyuan primary melts have Fo values of 94.2 and 91.3, respectively. The melt $Fe^{3+}/\Sigma Fe$ ratios can be calculated by

the equation ($Fe^{3+}/\Sigma Fe = 0.1386e^{0.3772X}$; X is $\Delta\log[fO_2]$ for the FMQ buffer; $R^2 = 0.94$) derived from Botcharnikov et al. (2005). The olivine-spinel oxybarometer yields log fO_2 values of ΔFMQ + 1.9 for Dali and ΔFMQ + 1.5 for Yanyuan lavas (Fig. 3c). Thus, the $Fe^{3+}/\Sigma Fe$ ratios of the Dali and Yanyuan lavas are 0.28 and 0.25, respectively.

For most of mantle-melt barometers, the thermodynamic basis is the well-known pressure dependence of Si activity in melt co-saturated in olivine and orthopyroxene (e.g., Lee et al., 2009; Plank and Forsyth, 2016; Putirka, 2008). However, silica-activity becomes much less sensitive to pressure changes above 3 GPa (Plank and Forsyth, 2016, Sun and Dasgupta, 2020), and hence the Si-activity barometer is more credible for spinel-peridotite melts. Sun and Dasgupta (2020) recently developed a new thermobarometer for silica-poor, CO_2-bearing melts saturated with garnet and olivine. Thus, the barometers of Lee et al. (2009) and Sun and Dasgupta (2020) are used to estimate the pressures of mantle melting that generated the Dali and Yanyuan lavas, respectively. We have used their correction schemes (including compositionally dependent $K_D[Fe/Mg]^{ol/liq}$) to estimate primary melt compositions. Nineteen samples with MgO > 9 wt.% were selected as starting compositions, and the barometer results are given in Table S1.

2.2. Olivine-spinel oxybarometer

The oxybarometer of Ballhaus et al. (1991) was used to calculate the fO_2 of the Dali and Yanyuan lavas. It is expressed as:

$$\Delta FMQ = 0.27 + 2505/T - 400P/T - 6\log(X^{ol}_{Fe}) - 3200(1 - X^{ol}_{Fe})^2/T + 2\log(X^{sp}_{Fe2+}) + 4\log(X^{sp}_{Fe3+}) + 2630(X^{sp}_{Al})^2/T \quad (1)$$

where ΔFMQ is the deviation of logfO_2 from the fayalite-magnetite-quartz (FMQ) buffer. X^{sp}_{Fe3+} and X^{sp}_{Al} represent the $Fe^{3+}/\Sigma R^{3+}$ and $Al/\Sigma R^{3+}$ ratios in spinel, X^{ol}_{Fe} and X^{sp}_{Fe2+} are the $Fe^{2+}/(Fe^{2+} + Mg)$ ratios in olivine and spinel, respectively. P is pressure in GPa, T is temperature in K. The olivines suitable for the application of this oxybarometer should have Fo > 85 (Ballhaus et al., 1991). The olivines containing spinels in studied samples have Fo contents varying from 86 to 94, which are all applicable to the equation. The spinel grains in this study are euhedral, fresh, and homogeneous, and they are enclosed within olivine (Fig. S2). Textures showing chemical disequilibrium, such as complex zoning, embayment, symplectite, and sieve texture, are not observed in spinel (Fig. S2).

The $Fe^{3+}/\Sigma Fe$ ratios of spinel based on EPMA data needs to be corrected before it can be used to calculate the fO_2 of magma (Cao et al., 2019; Davis et al., 2017; Wood and Virgo, 1989). Here, nine spinel standards (MHP79-4, BAR8601-9, BAR8601-10, DB8803-3, IM8703, KLB8320, Mo103, Mo4230-16, and Vi86-1; Wood and Virgo, 1989) were analyzed using EPMA and the $Fe^{3+}/\Sigma Fe$ of the standards was calculated based on the perfect stoichiometry (Droop, 1987). The results are compared with those obtained by Mössbauer spectroscopy (after Wood and Virgo, 1989), showing that the EPMA results are systematically lower than those by Mössbauer Spectroscopy (Table S7 and Fig. S6a). The same feature was also reported by previous studies (Cao et al., 2019; Davis et al., 2017; Wood and Virgo, 1989). The difference between the two methods can be expressed as $\Delta Fe^{3+}/\Sigma Fe^{Möss-EPMA}$, and the $Fe^{3+}/\Sigma Fe$ of our spinel samples based on EPMA results can be corrected by equation:

$$\Delta Fe^{3+}/\Sigma Fe^{Möss-EPMA} = A \times Cr\# + B \quad (2)$$

where A and B refers to the slope and intercept of the best fit line that defines the relationship between $\Delta Fe^{3+}/\Sigma Fe^{Möss-EPMA}$ and the Cr# of spinel (Davis et al., 2017; Wood and Virgo, 1989).

The best fit line of $\Delta Fe^{3+}/\Sigma Fe^{Möss-EPMA}$ and the Cr# of nine spinel standards yielded the slope A of -0.081 and intercept B of 0.055 (Fig. S6b). This equation was then used to correct the $Fe^{3+}/\Sigma Fe$ of the spinels from the Dali and Yanyuan lavas.

For the olivine-spinel oxybarometer, the temperature is given by the Al-in-olivine-spinel thermometer based on the partitioning of Al between coexisting olivine and spinel (Coogan et al., 2014). The pressure is calculated by the clinopyroxene-liquid equilibria barometer (Neave and Putirka, 2017). We used only clinopyroxenes in Fe/Mg exchange equilibrium ($K_D[Fe/Mg]^{cpx/liq}$ = 0.28 ± 0.08; Putirka, 2008) with host rocks. In this case, the whole-rock compositions of the host rocks were used as the melt compositions. This barometer yields pressures of 3.8 ± 1.0 kbar (1σ, n = 20) for Dali and 5.8 ± 1.0 kbar (1σ, n = 54) for Yanyuan clinopyroxenes (Fig. S5a). Although the crystallization pressures of olivine and clinopyroxene may be slightly different, a variation of ±10 kbar can cause a maximum ΔFMQ error of ±0.25 based on Eq. (1). Thus, the narrow pressure variation cannot significantly influence fO_2 calculation. The Dali and Yanyuan spinel grains have corrected $Fe^{3+}/\Sigma Fe$ ratios of 0.16–0.38 (Table S4). Therefore, the uncertainty in fO_2 relative to the FMQ buffer contributed by the spinel analysis is less than 0.4 log units (Davis et al., 2017), which is within the precision of oxybarometer (Ballhaus et al. 1991). The oxybarometer results are given in Table S4.

2.3. Ca-in-olivine hygrometer

The magma H_2O contents can be estimated by the hygrometer of Gavrilenko et al. (2016) based on the partition coefficients ($D_{CaO}^{ol/liq}$) of CaO between olivine and its equilibrium liquid:

$$H_2O\ (wt\%) = 397 \times (0.00042 \times MgO_{liq} + 0.0196 - D_{CaO}^{ol/liq}) \quad (3)$$

where MgO_{liq} is the MgO (wt%) contents of liquid in equilibrium with olivine.

We used only olivines in Fe/Mg exchange equilibrium ($K_D[Fe/Mg]^{ol/liq}$ = 0.30 ± 0.03; Roeder and Emslie (1970)) with host rocks (Fig. S4). In this case, the whole-rock compositions of the host rocks were regarded as nominal liquid compositions. Although the Dali lavas experienced assimilation and digestion of high-$\delta^{18}O$ diabasic lithic fragments, this self-cannibalization of cognate mafic rocks has little effect on CaO contents of basalts because these fragments have similar CaO contents to the lavas (Fig. 2b). The total uncertainty in magmatic H_2O content inferred from $D_{CaO}^{ol/liq}$ and MgO is ± 1.8 wt% (1σ). The hygrometer results are given in Table S6.

2.4. REE modeling for non-modal batch melting of phlogopite peridotite

Rare earth elements (REE) are used to qualitatively understand the difference in melting depth between the Dali and Yanyuan lavas. Magma composition is a function of mantle composition, the nature of the melting process, and degree and depth of partial melting. We use a non-modal batch melting equation:

$$C_L/C_0 = 1/(D + F[1 - P]) \quad (4)$$

where C_0 is the initial concentration of REE in the mantle source, C_L is its concentration in the liquid, F is the melt fraction, D is the average distribution coefficient for the mantle phases weighted by their respective mass fractions before the onset of melting, and P is the average distribution coefficient for the mantle phases weighted by their respective contribution to the melt. We use the following mantle melting proportions for phlogopite-bearing spinel harzburgite and garnet lherzolite, respectively:

0.70 Phl + 1.24 Opx + 0.05 Sp = 0.99 Ol + 1.00 melt (Condamine and Médard, 2014)

0.59 Phl + 0.52 Cpx + 0.18 Grt = 0.06 Ol + 0.23 Opx + 1.00 melt (Condamine et al., 2016) where the abbreviations for the minerals are: Ol, olivine; Cpx, clinopyroxene; Opx, orthopyroxene; Sp, spinel; Grt, garnet; Phl, phlogopite. The peridotites have a mineralogical composition: (1) 63% Ol, 25% Opx, 10 % Phl and 2% Sp (spinel-harzburgite; Condamine and Médard, 2014); (2) 57.5% Ol, 15.4% Opx, 8.9% Cpx, 9.7 % Phl and 8.6% Grt (garnet-lherzolite; Condamine et al., 2016). Partition coefficients (D) vary with pressure, temperature and liquid composition, and this limits the reliability of partial melting models as the choice of values is always somewhat subjective. Here we have attempted to be more objective by using the averages of appropriate D values provided by Pilet et al. (2011).

The REE compositions of continental lithospheric mantle are highly heterogeneous due to mantle metasomatism, but both the average and median compositions of 375 peridotite xenoliths from global continental basalts have light REE-enriched patterns (McDonough, 1990). It is difficult to define the REE contents (C_0) in the mantle sources of the SYC lavas. Here, we assume that their mantle sources have the REE contents of average peridotites (McDonough, 1990). To reproduce the variation in REE patterns of our samples, another source with higher REE content and Sm/Yb ratio is also assumed based on the standard deviations of the average values (McDonough, 1990). All other modeling parameters and results are given in Table S8.

2.5. The effect of fractional crystallization on $\delta^{18}O$ (Fig. 3c-d)

We have modeled the effect of olivine fractionation on melt $\delta^{18}O$ values using the Rayleigh formula:

$$\delta^{18}O_{melt} = \delta^{18}O_{melt}{}^{0} + 1000 \times (\alpha - 1) \ln f \quad (5)$$

where $\delta^{18}O_{melt}{}^{0}$ is the initial $\delta^{18}O$ value of the primary magma, α is olivine–melt oxygen isotope fractionation factor, and *f* is the fraction of remaining melt. The magma is in equilibrium with the instantaneous olivine ($\delta^{18}O_{olivine}$) by the following relationship:

$$\delta^{18}O_{olivine} - \delta^{18}O_{melt} \approx 1000 \times \ln \alpha \quad (6)$$

Combination of Eq. (5) and (6) yields:

$$\delta^{18}O_{olivine} = \delta^{18}O_{olivine}{}^{0} + 1000 \times (\alpha - 1) \ln f \quad (7)$$

where $\delta^{18}O_{olivine}{}^{0}$ is the $\delta^{18}O$ value of olivine in equilibrium with the primary magma. The fractionation factor α is slightly affected by decreasing temperature in a fractionating magma; we simplified this effect using constant $\alpha_{olivine\text{-}basalt}$ of 0.9993 which is a representative average value for MgO-rich magmas crystallizing in temperature range of 1500 to 1200 ℃ (Zhao and Zheng 2003). Including pyroxene and An-rich plagioclase in the fractionating mineral assemblage would make the increase of $\delta^{18}O$ less significant as both minerals have $\alpha_{mineral\text{-}basalt}$ values that are closer to 1 (and more than 1 for An-rich plagioclase) than $\alpha_{olivine\text{-}basalt}$ value (Zhao and Zheng 2003). Thus, our model can be considered to illustrate the maximum effect of fractional crystallization. Starting composition was the Dali sample DL07-5 in equilibrium with an olivine grain that has Fo of 94, NiO of 0.6 wt.%, and $\delta^{18}O$ of 5.2 ‰.

A series of olivine and basalt compositions were then calculated from the starting basalt as follows: (1) the composition of equilibrium olivine was obtained using $K_D(Fe/Mg)^{ol/liq}$ and $D_{Ni}{}^{oliv/liq}$; (2) a more evolved basalt composition was calculated by subtracting equilibrium olivine from the primitive magma in 1% decrements; (3) steps (1) and (2) were repeated obtain more evolved (i.e., low-Mg) basalt and olivine. The Fe-Mg exchange coefficient ($K_D[Fe/Mg]^{ol/liq}$) and partition coefficient ($D_{Ni}{}^{ol/liq}$) of Ni between olivine and liquid were obtained by using the

equations of Tamura et al. (2000):

$$K_D(Fe/Mg)^{ol/liq} = 0.253 + 0.0034 \times (MgO + 0.33FeO)_{liq} \quad (8)$$

$$D_{Ni}^{oliv/liq} = (Fo/100) \times \exp(0.355 - 1.263\ln[MgO^{liq}]) \quad (9)$$

where MgO and FeO are oxide molar contents (mol%). The final results are shown in Table S9.

Text S3. Data sources in Fig. 2–3

Fig. 2a and 2b show the experimental partial melts of harzburgite (± phlogopite; 1–2 GPa; Condamine and Medard, 2014; Falloon and Danyushevsky, 2000; Pickering-Witter and Johnston, 2000), lherzolite (± phlogopite; 3–5 GPa; Condamine et al., 2016; Davis and Hirschmann, 2013; Hirose and Kushiro, 1993; Kushiro, 1996; Walter, 1998), and lherzolite (+ CO_2; 3–5 GPa; Dasgupta et al., 2007; 2013; Dvir and Kessel, 2017; Tenner et al., 2012) for comparison. Also shown are low-Ca boninites of the Izu-Bonin Arc (Shervais et al., 2021) and potassic lavas from previous studies (Guo et al., 2005; Huang et al., 2010).

Fig. 3a and 3b show olivines from MORB (Sobolev et al., 2007), Italian lamproites (Ammannati et al., 2016), arc lavas (Gavrilenko et al., 2016; Kamenetsky et al., 2006), and low-Ca boninites (Kamenetsky et al., 1997; 2002) for comparison.

Fig. 3c shows the olivine–spinel pairs from MORB, arc lavas, and, boninites (Ballhaus et al., 1991; Dare et al., 2009) for comparison. The logfO_2(ΔFMQ) values were calculated by the olivine-spinel oxybarometer (Ballhaus et al., 1991).

Fig. 3d shows the inferred magmatic H_2O contents in MORB and arc basalts (Gavrilenko et al., 2016; Hong et al., 2020) based on the partition coefficients of CaO between olivines and their equilibrium melts.

Supplemental Figure Captions

Fig. S1. Photomicrographs of the Dali (a–d) and Yanyuan (e–g) lavas. (a–c) Olivine phenocrysts and diabasic lithic fragments (outlined by the red line) that mainly consist of fine-grained feldspar and clinopyroxene. (d–g) Large phenocrysts in the Dali lavas and small phenocrysts in the Yanyuan lavas. All were taken under cross-polarized light except for (b) showing a photomicrograph of (a) under plane-polarized light, and for (g) showing a back-scattered electron (BSE) image. Ol = olivine, Cpx = clinopyroxene, Phl = phlogopite, LF = lithic fragments.

Fig. S2. (a–o) BSE images of olivine grains with spinel (Sp) inclusions. The yellow rectangles in Fig. S2a–e outline the areas highlighted in Fig. S2f–k that show the euhedral, fresh, and homogeneous spinel inclusions. (p–q) Transmitted light images of olivine grains with oval melt inclusions (MI). (r–s) A euhedral, low-CaO (<0.1 wt%) olivine phenocryst and its compositional profile. Fig. S2n–o are from the Yanyuan samples and the others are from the Dali samples. The red numbers in Fig. S2l–o represent Fo and $\delta^{18}O$ values and the green ellipses next to them are the positions of ion microprobe analyses of O isotopes. The red scale bars in the lower right corner of Fig. S2f–k is 10 μm long and the others are 100 μm long.

Fig. S3. (a) P_2O_5 versus Fo content in olivine. (b) Whole-rock P_2O_5 versus 100*Mg/(Mg+Fe^{2+}). The whole-rock Fe^{2+} contents were calculated using $Fe^{3+}/\Sigma Fe$ = 0.28 and 0.25 for the Dali and Yanyuan lavas, respectively.

Fig. S4. (a) Olivine–melt Fe/Mg equilibrium diagram. The Fe-Mg exchange coefficient ($K_D[Fe/Mg]^{ol/liq}$ = 0.30 ± 0.03) between olivine and melt are well constrained by Roeder and Emslie (1970). The whole-rock compositions of the host rocks were regarded as nominal melt compositions. The whole-rock Fe^{2+} contents were calculated using $Fe^{3+}/\Sigma Fe$ = 0.28 and 0.25 for the Dali and Yanyuan lavas, respectively. Arrows indicate the relative effects of olivine accumulation and differentiation on Fe/Mg equilibrium. (b) Melt H_2O contents versus $K_D[Fe/Mg]^{ol/liq}$. Error bars are ± 1σ.

Fig. S5. (a) Crystallization pressure (kbar) of clinopyroxenes estimated using the barometer of Neave and Putirka (2017). (b) TiO_2 versus 100*Mg/(Mg+Fe) in clinopyroxenes. The clinopyroxenes in the Dali lavas and their hosted lithic fragments have similar compositions, but they have lower TiO_2 contents than those in the Yanyuan lavas at a given 100*Mg/(Mg+Fe), a difference also shown by their corresponding host rocks (Table S1).

Fig. S6. (a) Correlation of $Fe^{3+}/\Sigma Fe$ for spinel standards based on EPMA and Mössbauer Spectroscopy data showing that the $Fe^{3+}/\Sigma Fe$ based on EPMA data are systematically lower than those determined by Mössbauer Spectroscopy. (B) Cr# versus $\Delta Fe^{3+}/\Sigma Fe$ (Möss−EPMA) for spinel standards. Mossbauer data are from Wood and Virgo (1989).

Supplemental Table Captions (Table S1–S9 as separate Excel files)

Table S1. Major (wt%, on a volatile-free basis) and trace (ppm) element data and melting pressures (GPa) for the Dali and Yanyuan lavas.

Table S2. Major and minor element (wt%) compositions of olivines from the Dali and Yanyuan lavas and monitoring standards (MongOl).

Table S3. Major element (wt%) compositions and crystallization pressures (kbar) of clinopyroxenes in the Dali and Yanyuan lavas.

Table S4. Major element (wt%) compositions of spinel inclusions in olivine and calculated fO_2 results of olivine–spinel pairs in the Dali and Yanyuan lavas.

Table S5. Oxygen isotopic data for olivines from the Dali and Yanyuan lavas and monitoring standards (06JY29).

Table S6. H_2O (wt%) contents in the Dali and Yanyuan lavas based on the partition coefficients of CaO between olivines and their host rocks.

Table S7. Major element (wt%) compositions of spinel standards determined by EPMA.

Table S8. Parameters for non-modal batch melting of phlogopite peridotite.

Table S9. Variations in major element and oxygen isotope of melts and their equilibrium olivines caused by olivine fractionation.

References

Ammannati, E., Jacob, D. E., Avanzinelli, R., Foley, S. F., and Conticelli, S., 2016, Low Ni olivine in silica-undersaturated ultrapotassic igneous rocks as evidence for carbonate metasomatism in the mantle: Earth and Planetary Science Letters, v. 444, p. 64-74.

Ballhaus, C., Berry, R., and Green, D., 1991, High pressure experimental calibration of the olivine-orthopyroxene-spinel oxygen geobarometer: implications for the oxidation state of the upper mantle: Contributions to Mineralogy and Petrology, v. 107, no. 1, p. 27-40.

Batanova, V. G., Sobolev, A. V., and Kuzmin, D. V., 2015, Trace element analysis of olivine: High precision analytical method for JEOL JXA-8230 electron probe microanalyser: Chemical Geology, v. 419, p. 149-157.

Bindeman, I., Gurenko, A., Sigmarsson, O., and Chaussidon, M., 2008, Oxygen isotope heterogeneity and disequilibria of olivine crystals in large volume Holocene basalts from Iceland: Evidence for magmatic digestion and erosion of Pleistocene hyaloclastites: Geochimica Et Cosmochimica Acta, v. 72, no. 17, p. 4397-4420.

Botcharnikov, R. E., Koepke, J., Holtz, F., McCammon, C., and Wilke, M., 2005, The effect of water activity on the oxidation and structural state of Fe in a ferro-basaltic melt: Geochimica Et Cosmochimica Acta, v. 69, no. 21, p. 5071-5085.

Cao, Y. H., Wang, C. Y., and Wei, B., 2019, Magma oxygen fugacity of Permian to Triassic Ni-Cu sulfide-bearing mafic-ultramafic intrusions in the central Asian orogenic belt, North China: Journal of Asian Earth Sciences, v. 173, p. 250-262.

Condamine, P., and Medard, E., 2014, Experimental melting of phlogopite-bearing mantle at 1 GPa: Implications for potassic magmatism: Earth and Planetary Science Letters, v. 397, p. 80-92.

Condamine, P., Medard, E., and Devidal, J. L., 2016, Experimental melting of phlogopite-peridotite in the garnet stability field: Contributions to Mineralogy and Petrology, v. 171, no. 11.

Coogan, L. A., Saunders, A. D., and Wilson, R. N., 2014, Aluminum-in-olivine thermometry of primitive basalts: Evidence of an anomalously hot mantle source for large igneous provinces: Chemical Geology, v. 368, p. 1-10.

Dare, S. A. S., Pearce, J. A., McDonald, I., and Styles, M. T., 2009, Tectonic discrimination of peridotites using fO(2)-Cr# and Ga-Ti-Fe-III systematics in chrome-spinel: Chemical Geology, v. 261, no. 3-4, p. 199-216.

Dasgupta, R., Hirschmann, M. M., and Smith, N. D., 2007, Partial melting experiments of peridotite CO2 at 3 GPa and genesis of alkalic ocean island basalts: Journal of Petrology, v. 48, no. 11, p. 2093-2124.

Dasgupta, R., Mallik, A., Tsuno, K., Withers, A. C., Hirth, G., and Hirschmann, M. M., 2013, Carbon-dioxide-rich silicate melt in the Earth's upper mantle: Nature, v. 493, no. 7431, p. 211-U222.

Davis, F. A., Cottrell, E., Birner, S. K., Warren, J. M., and Lopez, O. G., 2017, Revisiting the

electron microprobe method of spinel-olivine-orthopyroxene oxybarometry applied to spinel peridotites: American Mineralogist, v. 102, no. 1-2, p. 421-435.

Davis, F. A., and Hirschmann, M. M., 2013, The effects of K2O on the compositions of near-solidus melts of garnet peridotite at 3 GPa and the origin of basalts from enriched mantle: Contributions to Mineralogy and Petrology, v. 166, no. 4, p. 1029-1046.

Droop, G. T. R., 1987, A general equation for estimating Fe3+ concentrations in ferromagnesian silicates and oxides from microprobe analyses, using stoichiometric criteria: Mineralogical Magazine, v. 51, no. 361, p. 431-435.

Dvir, O., and Kessel, R., 2017, The effect of CO2 on the water-saturated solidus of K-poor peridotite between 4 and 6 GPa: Geochimica Et Cosmochimica Acta, v. 206, p. 184-200.

Falloon, T. J., and Danyushevsky, L. V., 2000, Melting of refractory mantle at 1 center dot 5, 2 and 2 center dot 5 GPa under, anhydrous and H2O-undersaturated conditions: Implications for the petrogenesis of high-Ca boninites and the influence of subduction components on mantle melting: Journal of Petrology, v. 41, no. 2, p. 257-283.

Gavrilenko, M., Herzberg, C., Vidito, C., Carr, M. J., Tenner, T., and Ozerov, A., 2016, A Calcium-in-Olivine Geohygrometer and its Application to Subduction Zone Magmatism: Journal of Petrology, v. 57, no. 9, p. 1811-1831.

Guo, Z. F., Hertogen, J., Liu, J. Q., Pasteels, P., Boven, A., Punzalan, L., He, H. Y., Luo, X. J., and Zhang, W. H., 2005, Potassic magmatism in western Sichuan and Yunnan Provinces, SE Tibet, China: Petrological and geochemical constraints on petrogenesis: Journal of Petrology, v. 46, no. 1, p. 33-78.

Hirose, K., and Kushiro, I., 1993, Partial Melting of Dry Peridotites at High-Pressures - Determination of Compositions of Melts Segregated from Peridotite Using Aggregates of Diamond: Earth and Planetary Science Letters, v. 114, no. 4, p. 477-489.

Hong, L. B., Xu, Y. G., Zhang, L., Liu, Z., Xia, X. P., and Kuang, Y. S., 2020, Oxidized Late Mesozoic subcontinental lithospheric mantle beneath the eastern North China Craton: A clue to understanding cratonic destruction: Gondwana Research, v. 81, p. 230-239.

Huang, X. L., Niu, Y. L., Xu, Y. G., Chen, L. L., and Yang, Q. J., 2010, Mineralogical and Geochemical Constraints on the Petrogenesis of Post-collisional Potassic and Ultrapotassic Rocks from Western Yunnan, SW China: Journal of Petrology, v. 51, no. 8, p. 1617-1654.

Isa, J., Kohl, I. E., Liu, M. C., Wasson, J. T., Young, E. D., and McKeegan, K. D., 2017, Quantification of oxygen isotope SIMS matrix effects in olivine samples: Correlation with sputter rate: Chemical Geology, v. 458, p. 14-21.

Kamenetsky, V. S., Crawford, A. J., Eggins, S., and Muhe, R., 1997, Phenocryst and melt inclusion chemistry of near-axis seamounts, Valu Fa Ridge, Lau Basin: insight into mantle wedge melting and the addition of subduction components: Earth and Planetary Science Letters, v. 151, no. 3-4, p. 205-223.

Kamenetsky, V. S., Elburg, M., Arculus, R., and Thomas, R., 2006, Magmatic origin of low-Ca olivine in subduction-related magmas: Co-existence of contrasting magmas: Chemical Geology, v. 233, no. 3-4, p. 346-357.

Kamenetsky, V. S., Sobolev, A. V., Eggins, S. M., Crawford, A. J., and Arculus, R. J., 2002, Olivine-enriched melt inclusions in chromites from low-Ca boninites, Cape Vogel, Papua New Guinea: evidence for ultramafic primary magma, refractory mantle source and enriched components: Chemical Geology, v. 183, no. 1-4, p. 287-303.

Kushiro, I., 1996, Partial Melting of a Fertile Mantle Peridotite at High Pressures: An Experimental Study Using Aggregates of Diamond, Earth Processes: Reading the Isotopic Code, p. 109-122.

Lee, C. T. A., Luffi, P., Plank, T., Dalton, H., and Leeman, W. P., 2009, Constraints on the depths and temperatures of basaltic magma generation on Earth and other terrestrial planets using new thermobarometers for mafic magmas: Earth and Planetary Science Letters, v. 279, no. 1-2, p. 20-33.

Li, X. H., Li, Z. X., Wingate, M. T. D., Chung, S. L., Liu, Y., Lin, G. C., and Li, W. X., 2006, Geochemistry of the 755 Ma Mundine Well dyke swarm, northwestern Australia: Part of a Neoproterozoic mantle superplume beneath Rodinia?: Precambrian Research, v. 146, no. 1-2, p. 1-15.

Li, X. H., Qi, C. S., Liu, Y., Liang, X. R., Tu, X. L., Xie, L. W., and Yang, Y. H., 2005, Petrogenesis of the Neoproterozoic bimodal volcanic rocks along the western margin of the Yangtze Block: New constraints from Hf isotopes and Fe/Mn ratios: Chinese Science Bulletin, v. 50, no. 21, p. 2481-2486.

McDonough, W. F., 1990, Constraints on the composition of the continental lithospheric mantle: Earth and Planetary Science Letters, v. 101, no. 1, p. 1-18.

Neave, D. A., and Putirka, K. D., 2017, A new clinopyroxene-liquid barometer, and implications for magma storage pressures under Icelandic rift zones: American Mineralogist, v. 102, no. 12, p. 2532-2532.

Pickering-Witter, J., and Johnston, A. D., 2000, The effects of variable bulk composition on the melting systematics of fertile peridotitic assemblages: Contributions to Mineralogy and Petrology, v. 140, no. 2, p. 190-211.

Pilet, S., Baker, M. B., Müntener, O., and Stolper, E. M., 2011, Monte Carlo Simulations of Metasomatic Enrichment in the Lithosphere and Implications for the Source of Alkaline Basalts: Journal of Petrology, v. 52, no. 7-8, p. 1415-1442.

Plank, T., and Forsyth, D. W., 2016, Thermal structure and melting conditions in the mantle beneath the Basin and Range province from seismology and petrology: Geochemistry Geophysics Geosystems, v. 17, no. 4, p. 1312-1338.

Putirka, K. D., 2008, Thermometers and barometers for volcanic systems: Reviews in Mineralogy and Geochemistry, v. 69, no. 1, p. 61-120.

Roeder, P., and Emslie, R., 1970, Olivine-liquid equilibrium: Contributions to mineralogy and petrology, v. 29, no. 4, p. 275-289.

Shervais, J. W., Reagan, M. K., Godard, M., Prytulak, J., Ryan, J. G., Pearce, J. A., Almeev, R. R., Li, H. Y., Haugen, E., Chapman, T., Kurz, W., Nelson, W. R., Heaton, D. E., Kirchenbaur, M., Shimizu, K., Sakuyama, T., Vetter, S. K., Li, Y. B., and Whattam, S., 2021, Magmatic Response to Subduction Initiation, Part II: Boninites and Related Rocks of the Izu-Bonin Arc From IOPD Expedition 352: Geochemistry Geophysics Geosystems, v. 22, no. 1.

Sobolev, A. V., Hofmann, A. W., Kuzmin, D. V., Yaxley, G. M., Arndt, N. T., Chung, S. L., Danyushevsky, L. V., Elliott, T., Frey, F. A., and Garcia, M. O., 2007, The Amount of Recycled Crust in Sources of Mantle-Derived Melts: Science, v. 316, no. 5823, p. 412-417.

Sun, C. G., and Dasgupta, R., 2020, Thermobarometry of CO2-rich, silica-undersaturated melts constrains cratonic lithosphere thinning through time in areas of kimberlitic magmatism: Earth and Planetary Science Letters, v. 550.

Tamura, Y., Yuhara, M., and Ishii, T., 2000, Primary arc basalts from Daisen volcano, Japan: Equilibrium crystal fractionation versus disequilibrium fractionation during supercooling: Journal of Petrology, v. 41, no. 3, p. 431-448.

Tang, G. Q., Su, B. X., Li, Q. L., Xia, X. P., Jing, J. J., Feng, L. J., Martin, L., Yang, Q., and Li, X. H., 2019, High-Mg# Olivine, Clinopyroxene and Orthopyroxene Reference Materials for In Situ Oxygen Isotope Determination: Geostandards and Geoanalytical Research, v. 43, no. 4, p. 585-593.

Tenner, T. J., Hirschmann, M. M., and Humayun, M., 2012, The effect of H2O on partial melting of garnet peridotite at 3.5 GPa: Geochemistry Geophysics Geosystems, v. 13.

Walter, M. J., 1998, Melting of garnet peridotite and the origin of komatiite and depleted lithosphere: Journal of Petrology, v. 39, no. 1, p. 29-60.

Wood, B. J., and Virgo, D., 1989, Upper Mantle Oxidation-State - Ferric Iron Contents of Lherzolite Spinels by Fe-57 Mossbauer-Spectroscopy and Resultant Oxygen Fugacities: Geochimica Et Cosmochimica Acta, v. 53, no. 6, p. 1277-1291.

Yang, Q., Xia, X., Zhang, W., Zhang, Y., Xiong, B., Xu, Y., Wang, Q., and Wei, G., 2018, An evaluation of precision and accuracy of SIMS oxygen isotope analysis: Solid Earth Sciences, v. 3, no. 3, p. 81-86.

Zhao, Z. F., and Zheng, Y. F., 2003, Calculation of oxygen isotope fractionation in magmatic rocks: Chemical Geology, v. 193, no. 1-2, p. 59-80.

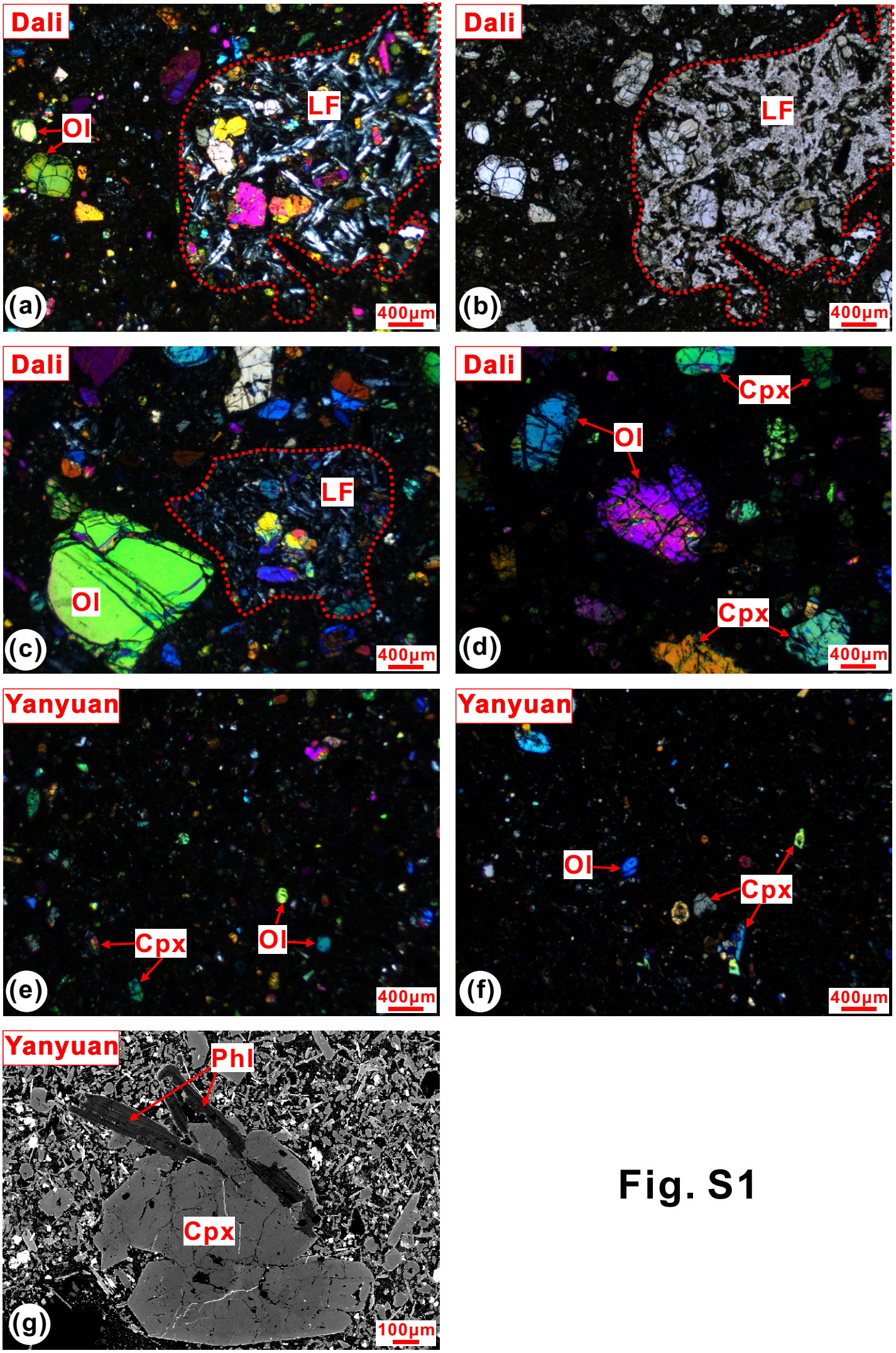
Dali
Ol
LF
(a)
400μm
Dali
LF
(b)
400μm
Dali
LF
Ol
(c)
400μm
Dali
Cpx
Ol
Cpx
(d)
400μm
Yanyuan
Cpx
Ol
(e)
400μm
Yanyuan
Ol
Cpx
(f)
400μm
Yanyuan
Phl
Cpx
(g)
100μm

Fig. S1

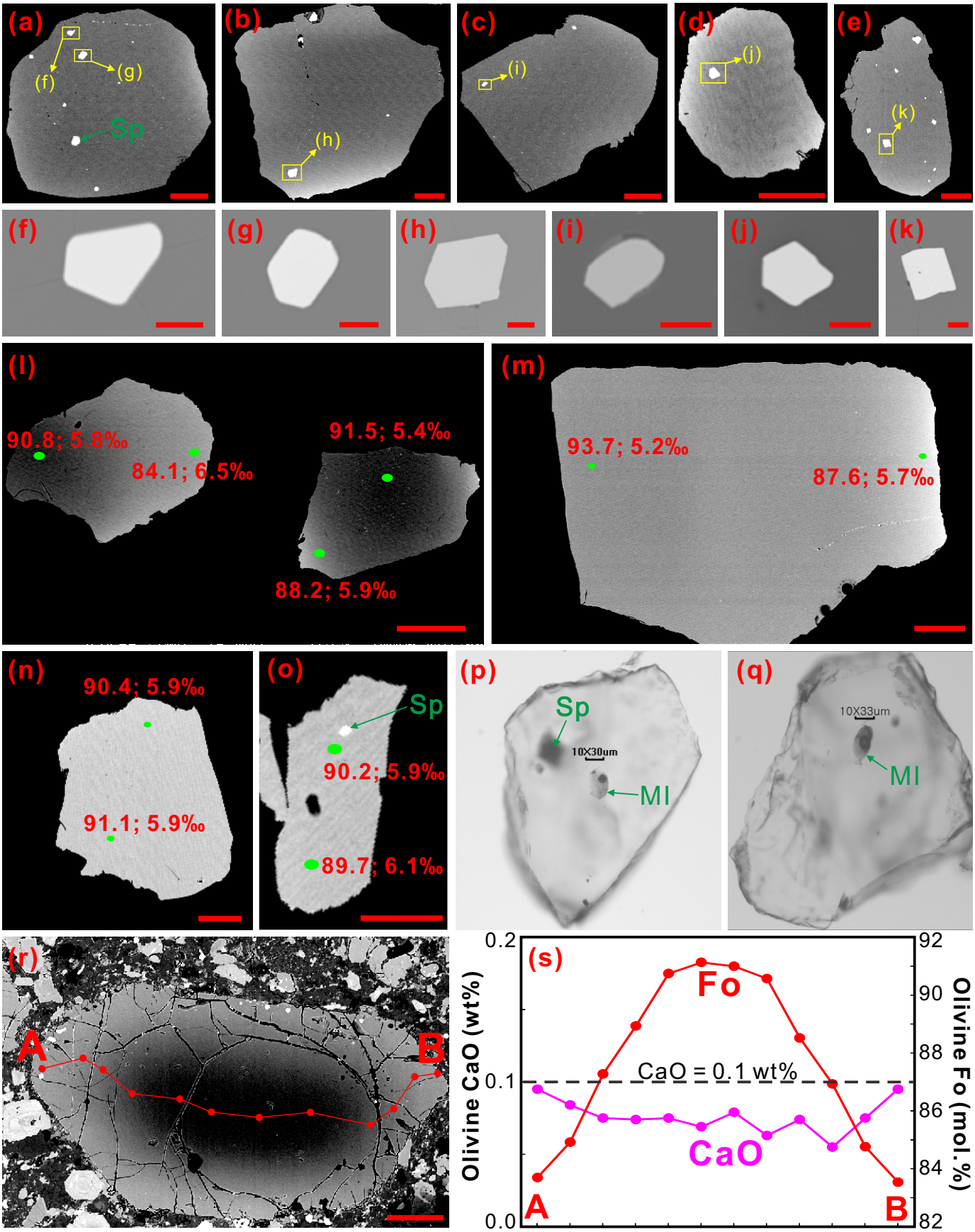
(a)
(f)
(g)
Sp
(b)
(h)
(c)
(i)
(d)
(j)
(e)
(k)
(f)
(g)
(h)
(i)
(j)
(k)
(l)
90.8; 5.8‰
84.1; 6.5‰
91.5; 5.4‰
88.2; 5.9‰
(m)
93.7; 5.2‰
87.6; 5.7‰
(n)
90.4; 5.9‰
91.1; 5.9‰
(o)
Sp
90.2; 5.9‰
89.7; 6.1‰
(p)
Sp
10X30um
MI
(q)
10X33um
MI
(r)
A
B
(s)
Fo
CaO = 0.1 wt%
CaO
A
B
Olivine CaO (wt%)
Olivine Fo (mol.%)
0.2
0.1
0.0
92
90
88
86
84
82

Fig. S2

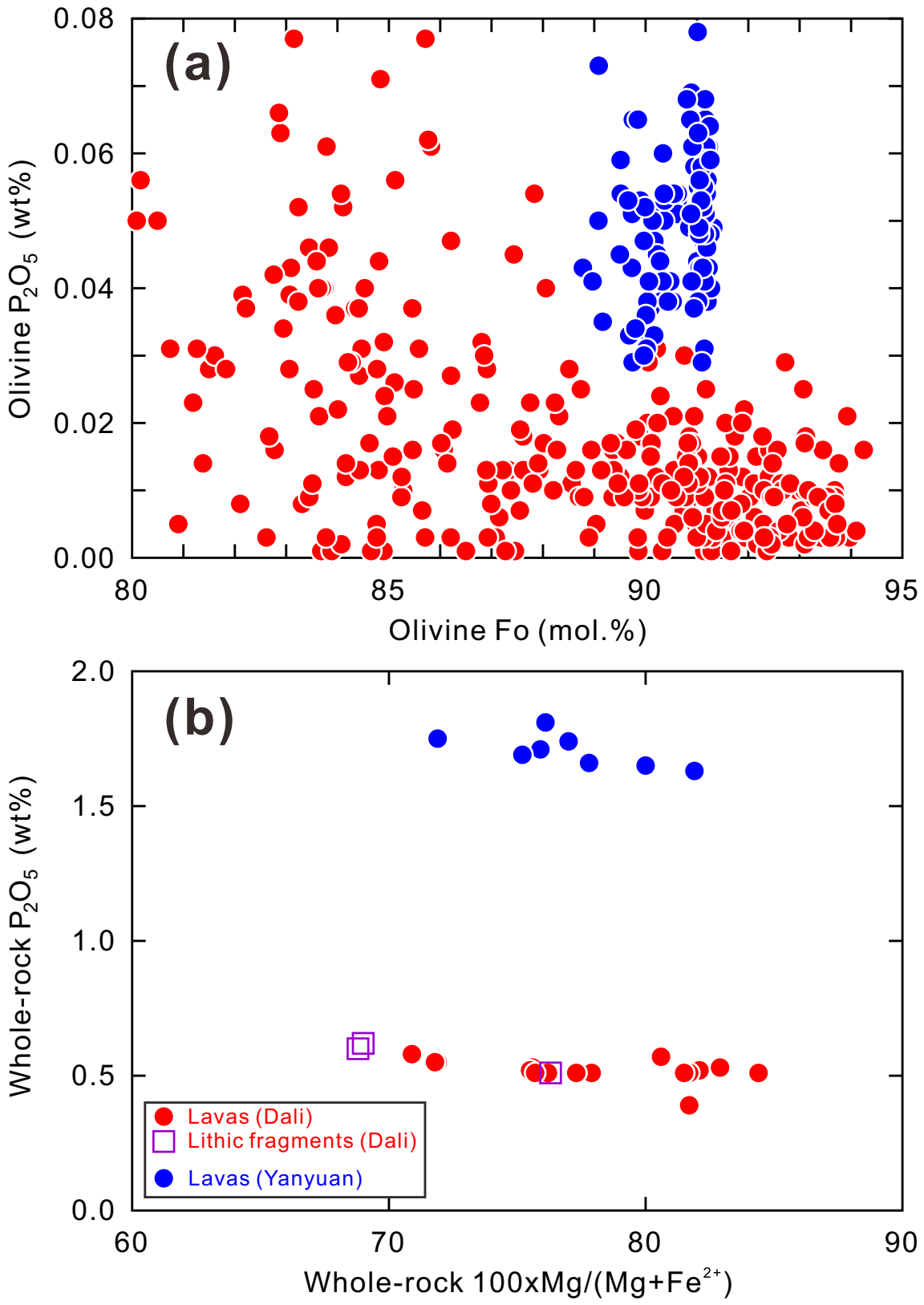
(a)
Olivine P_2O_5 (wt%)
0.08
0.06
0.04
0.02
0.00
80
85
90
95
Olivine Fo (mol.%)
(b)
Whole-rock P_2O_5 (wt%)
2.0
1.5
1.0
0.5
0.0
60
70
80
90
Whole-rock 100xMg/(Mg+Fe^{2+})
Lavas (Dali)
Lithic fragments (Dali)
Lavas (Yanyuan)

Fig. S3

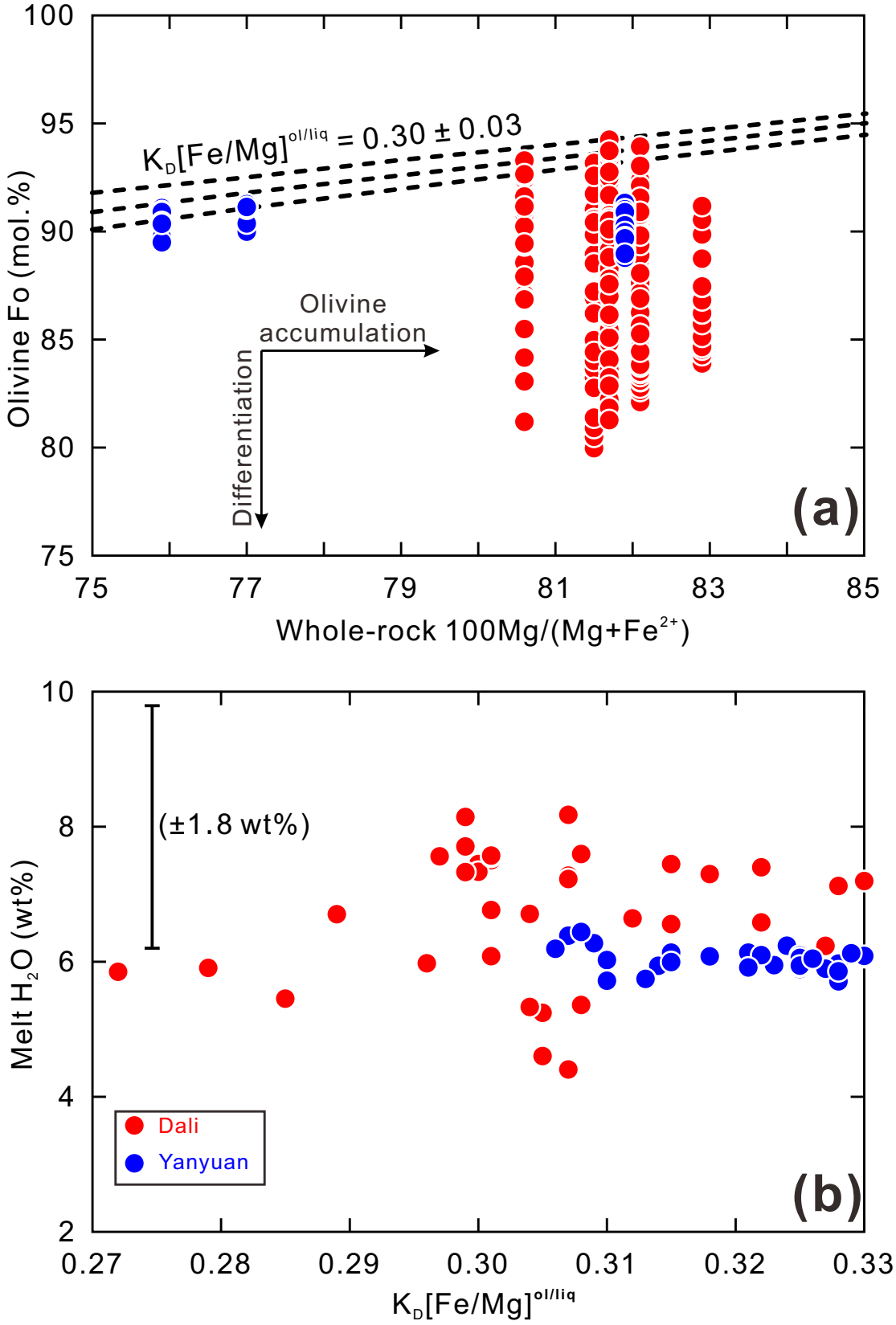
100
95
90
85
80
75
Olivine Fo (mol.%)
$K_D[Fe/Mg]^{ol/liq}$ = 0.30 ± 0.03
Olivine accumulation
Differentiation
(a)
75
77
79
81
83
85
Whole-rock 100Mg/(Mg+Fe^{2+})
10
8
6
4
2
Melt H_2O (wt%)
(±1.8 wt%)
Dali
Yanyuan
(b)
0.27
0.28
0.29
0.30
0.31
0.32
0.33
$K_D[Fe/Mg]^{ol/liq}$

Fig. S4

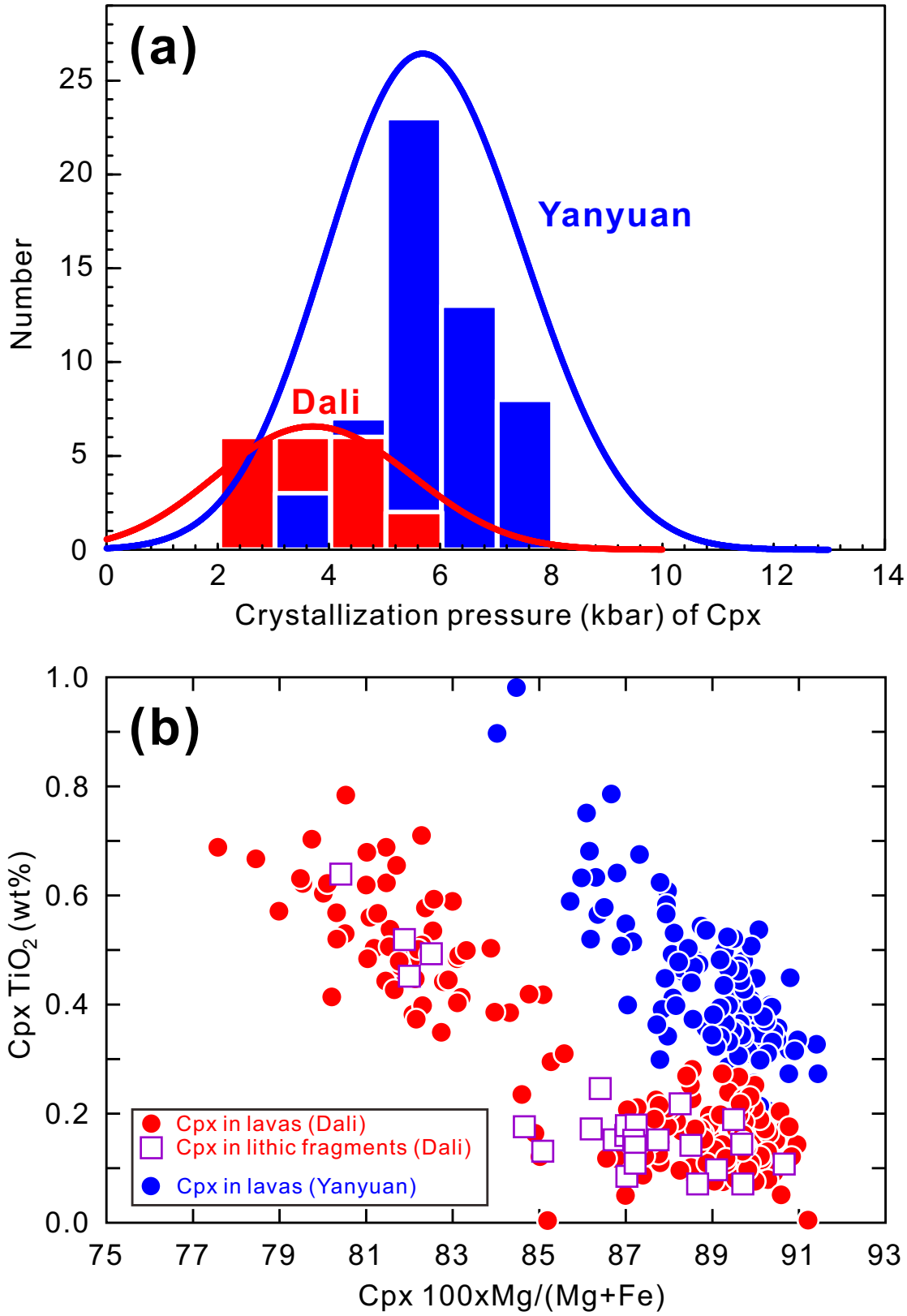
(a)
Yanyuan
Dali
Number
0
5
10
15
20
25
0
2
4
6
8
10
12
14
Crystallization pressure (kbar) of Cpx
(b)
Cpx TiO2 (wt%)
0.0
0.2
0.4
0.6
0.8
1.0
75
77
79
81
83
85
87
89
91
93
Cpx 100xMg/(Mg+Fe)
Cpx in lavas (Dali)
Cpx in lithic fragments (Dali)
Cpx in lavas (Yanyuan)

Fig. S5

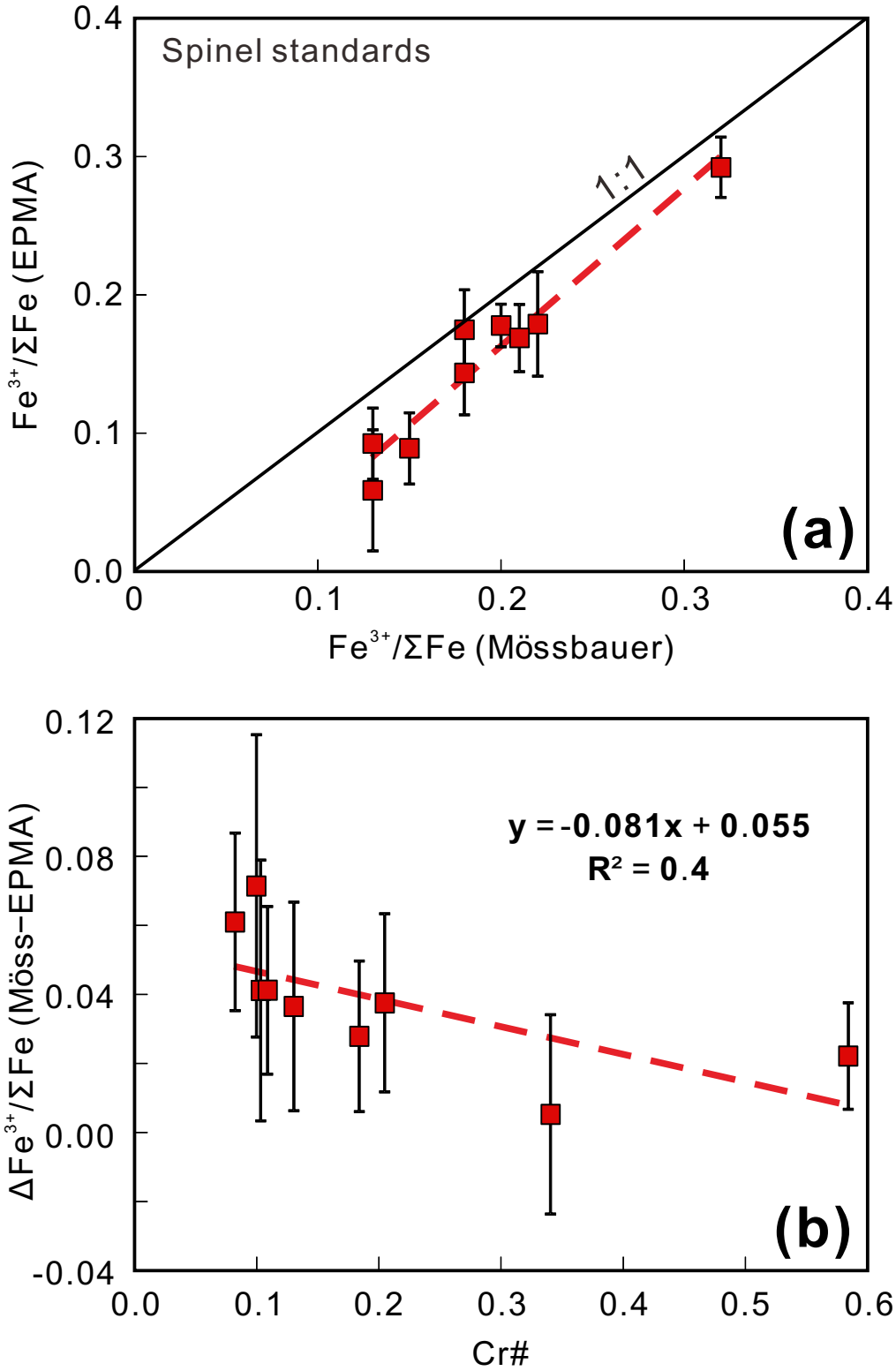
Spinel standards
1:1
(a)
0.4
0.3
0.2
0.1
0.0
0
0.1
0.2
0.3
0.4
Fe3+/ΣFe (EPMA)
Fe3+/ΣFe (Mössbauer)
y = -0.081x + 0.055
R² = 0.4
(b)
0.12
0.08
0.04
0.00
-0.04
0.0
0.1
0.2
0.3
0.4
0.5
0.6
ΔFe3+/ΣFe (Möss−EPMA)
Cr#

Fig. S6